Scientific Research Publishing

Journal of Modern Physics, 2026, 17(7), 888-904
https://www.scirp.org/journal/jmp
ISSN Online: 2153-120X
ISSN Print: 2153-1196

Sputtered Transport Layers Enabling Ambient-Air Processed $CsPbI_3$ Perovskite Solar Cells

Shamik Datta[1], Md Abdul Kuddus Sheikh[1*], Md Shazarul Islam[1], Mohammed Jasim Uddin[2], Hasina Huq[1*]

[1]Department of Electrical and Computer Engineering, The University of Texas Rio Grande Valley, Edinburg, TX, USA
[2]Department of Chemistry, The University of Texas Rio Grande Valley, Edinburg, TX, USA
Email: *mdabdul.kuddussheikh@utrgv.edu, *hasina.huq@utrgv.edu

How to cite this paper: Datta, S., Sheikh, M.A.K., Islam, M.S., Uddin, M.J. and Huq, H. (2026) Sputtered Transport Layers Enabling Ambient-Air Processed $CsPbI_3$ Perovskite Solar Cells. *Journal of Modern Physics*, **17**, 888-904.
https://doi.org/10.4236/jmp.2026.177039

Received: December 10, 2025
Accepted: July 20, 2026
Published: July 23, 2026

Abstract

Perovskite solar cells offer promising efficiency compared to traditional technologies. In this study, NiO_x and ZnO were employed as charge transport layers using a magnetron sputtering process within a p-i-n architecture (ITO-/NiO_x/$CsPbI_3$/ZnO/Au). This approach produced uniform, low-defect interfaces and supports low-temperature, scalable fabrication suitable for flexible substrates. Our investigation, using techniques such as X-Ray Diffraction (XRD), UV-Visible spectroscopy, Scanning Electron Microscopy (SEM), and Atomic Force Microscope (AFM), revealed the formation of uniform layers deposited by the magnetron sputtering process. The photoactive $CsPbI_3$ layer was deposited via a spin coating solution process. UV-Visible spectroscopy revealed strong absorbance in the wavelength range of 400 - 750 nm, corresponding to a band gap of 1.67 eV. XRD analysis confirmed the crystalline structure of both transport and active layers. Surface morphology studies revealed that $CsPbI_3$ formed large grains with good coverage, which contributed to improved device performance. AFM analysis revealed uniform surface coverage with low surface roughness values of 0.7 nm and 3.4 nm for NiO_x and ZnO, respectively. The best-performing device achieved a power conversion efficiency of 7.8%, with an open-circuit voltage of 0.82 V, a short-circuit current density of 14.25 mA/cm^2, and a fill factor of 67%. These results demonstrate the potential of combining sputter-deposited transport layers with solution-processed perovskites for efficient, scalable photovoltaic devices.

Keywords

Perovskites, Thin Films, Surface Morphology, Solar Cells, Device Efficiency

1. Introduction

Solar cells (SCs) are devices that convert solar energy into electrical power and are central to sustainable energy technologies. Traditional SCs are predominantly silicon (Si)-based, which currently achieve power conversion efficiencies (PCE) up to ~26% under standard test conditions [1] [2]. However, their performance remains limited by the Shockley-Queisser limit (~33%) and is further constrained by the high manufacturing costs and energy-intensive fabrication processes [3]. These limitations have driven extensive research into alternative semiconducting materials that are cost-effective and capable of achieving high efficiency [4].

In recent years, perovskite solar cells (PSCs) have emerged as promising alternatives to traditional silicon-based photovoltaics due to their excellent optoelectronic properties, low processing temperatures, and potential for high efficiency [5]-[10]. Yet, issues such as phase instability, lead toxicity, and environmental degradation remain significant obstacles [11] [12]. Among these, all-inorganic perovskites like cesium lead iodide ($CsPbI_3$) have attracted attention for their superior thermal stability compared to their organic-inorganic counterparts [13]-[15]. Despite their high efficiency, lead-based perovskites suffer from phase instability and lead toxicity, motivating the development of environmentally benign lead-free alternatives such as $MAGeI_3$ that can offer comparable optoelectronic properties [16]. Additionally, $CsPbI_3$ metastable black phase transitioning to the yellow δ-phase under ambient conditions, strategies such as careful compositional engineering, humidity-assisted synthesis, encapsulation strategies, and surface treatments to stabilize the photoactive *α*-phase and mitigate toxicity [17]. For instance, Wang *et al*. demonstrated that compositional engineering and humidity-assisted synthesis effectively stabilize the photoactive *α*-phase of $CsPbI_3$ [18], while Jiang *et al*. reported that encapsulation strategies using polymer barriers significantly reduce the environmental risk of lead leakage [19] [20]. Besides $CsPbI_3$, several cesium-based perovskite absorbers such as $CsSnI_3$, mixed-halide $CsSnI_{3-x}Br_x$, double perovskites (e.g., $Cs_2AgBiBr_6$), and bismuth-based $Cs_3Bi_2I_9$ have been proposed as lead-free alternatives [21]-[24]. However, these materials often suffer from issues including Sn^{2+} oxidation, indirect band gaps, low carrier mobility, or limited absorption, leading to relatively modest device efficiencies. In contrast, $CsPbI_3$ offers a near-optimal bandgap, strong light absorption, and superior charge-transport properties, making it a suitable benchmark absorber for evaluating sputtered transport layers and ambient-processed device architectures in this work.

In our study, we tackled issues of interfacial instability and scalability by implementing vacuum-compatible sputter-deposited NiO_x as the hole transport layer (HTL) and ZnO as the electron transport layer (ETL) in a p-i-n architecture ($ITO/NiO_x/CsPbI_3/ZnO/Au$), which provided uniform, dense, defect-suppressing interfaces, excellent barrier properties, and supported low-temperature and scalable processing. Unlike prior studies integrating sputtered NiO_x/ZnO with $CsPbI_3$ that rely on controlled environments or post-deposition recovery, this work demonstrates ambient-air processing compatibility of $CsPbI_3$ with sputtered oxide transport

layers. The incorporation of a PAN interfacial treatment in this work enables stable oxide-perovskite integration by alleviating sputter-induced interface degradation, emphasizing process robustness rather than optimized efficiency. This strategy aligns with findings by Tan *et al*., who emphasized the importance of scalable deposition techniques for large-area PSCs [25], and Xie *et al*., who highlighted the advantages of combining vapor-deposited contacts with solution-processed perovskites for improved reproducibility [26]. Moreover, Hwang *et al*. demonstrated that sputter-deposited NiO_x enables uniform, pinhole-free films with enhanced hole extraction, making it suitable for scalable perovskite device fabrication [27]. Similarly, Kim *et al*. and Jariwala *et al*. reported that sputtering-based transport layer deposition improves film uniformity and device reproducibility while being compatible with industrial-scale processing [28] [29]. On the other hand, the photoactive $CsPbI_3$ layer, deposited via a spin coating solution process, revealed large grains with good coverage, which contributed to improved device performance. In addition, the perovskite absorber is completely fabricated under ambient conditions, underscoring its environmental stability and potential for scalable production. The best-performing device achieved a power conversion efficiency of 7.8%, with an open-circuit voltage of 0.82 V, a short-circuit current density of 14.25 mA/cm^2, and a fill factor of 67%. Unlike most air-processed $CsPbI_3$ reports relying on solution-based contacts, our perovskite film withstands sequential vacuum sputtering of NiO_x and ZnO oxide layers as well as metal deposition while maintaining a low dark current (~5 nA/cm^{-2}), with the low surface roughness of sputtered NiO_x (~0.7 nm) and ZnO (~3.4 nm) correlating with this excellent sputter compatibility. These results demonstrate the potential of combining sputter-deposited transport layers with solution-processed perovskites for efficient, scalable photovoltaic devices.

2. Experimental and Methodology

Materials: N, N-dimethylformamide (DMF, 99.99%), Dimethyl Sulfoxide (DMSO, 99.5%), Isopropanol (99.99%), Lead Iodide (PbI_2, 99.999%), Cesium Iodide (CsI, 99.9%), and Polyacrylonitrile (PAN, Mw = 150,000) were purchased from Sigma-Aldrich. Dimethylammonium Iodide (DMAI, 99.99%) and Sodium Fluoride (NaF, 99%) were purchased from Great Cell Solar Materials. Sputtering targets NiO_x (99.99%) and ZnO (99.99%) were purchased from Himet-Materials. The ITO-coated patterned glass substrates were purchased from Ossila Corporation. All materials were used without further purification.

Preparation of the substrates: The ITO glass substrates were meticulously washed with detergent and deionized water for 15 minutes each. Later, the substrates were successively cleaned in an ultrasonic bath with acetone and isopropanol for 20 min each. To increase the wettability of the substrates, all the substrates were subjected to ultraviolet-ozone treatments for 25 minutes.

Deposition of transport layer: NiO_x thin films were deposited using a modified RF magnetron sputtering system with a high-purity NiO_x target (99.99%, 2" dia ×

0.25" thick) installed at the cathode [29]-[31]. Unlike conventional DC sputtering with Ni and oxygen gas, a pure NiO_x target was used, and depositions were carried out on pSi wafers, amorphous glass, and ITO-coated glass substrates. Prior to deposition, substrates were cleaned in argon plasma for 20 minutes at 0.20 Pa and 400 V. During deposition, substrates rotated at 35 rpm, placed 10 cm from the target, under 10 mTorr pressure, 60 W RF power, and 10 sccm Ar flow. ZnO thin films were also deposited at room temperature on ITO glass using standard RF sputtering with a 5 cm ZnO target, 75 W RF power, 1 Pa pressure, and 15 sccm Ar flow. All processes were performed in the AJA magnetron sputtering system under a base pressure of 10^{-6} Pa.

Deposition of active layer: Perovskite deposition recipe was explored and optimized using several reported techniques [32]-[35]. For PAN-treated $CsPbI_3$ films, 1.0 M precursor solution at a molar ratio 1:1:1 of CsI, PbI_2, DMAI, and 3 mg NaF was dissolved in DMF, and PAN (65 mg in 0.5 mL DMF) was added before spin coating with a spin rate of 2500 rpm for 30 s onto UV/O_3-treated NiO_x/ITO substrates, followed by annealing at 210˚C for 20 min.

Deposition of top electrode: Gold (Au) was deposited on both the working and counter electrodes using a DC magnetron sputtering system. To define the deposition areas, custom masks were created with a 3D printer. Prior to coating, the substrates underwent a preparation process involving a bias strike and a bias clean. The bias strike was performed using 30 W of RF power at 4 Pa for 10 seconds, followed by a bias clean at 50 W of RF power under a lower pressure of 5 mT. After preparation, the Au target was struck using 50 W of DC power at 30 mT for 10 seconds. Since metal thin film deposition generally takes less time than non-metals, the coating duration was limited to 60 seconds, with the argon gas flow rate maintained at 15 sccm throughout the process.

Measurement and characterization: Surface morphology of the samples was characterized using SEM 148 (ZEISS Sigma VP). The surface roughness of the films was measured by a profilometer (Mahr Mcsurf 300 C). The thickness of the films was measured by using an atomic force microscope (AFM, Veeco-3100). XRD analyses of the film samples were characterized using a Brucker D-8 XRD with Cu Kα X-ray 136 source apparatus using a step size of 0.04˚ with a scan range of 30˚ - 70˚. Devices, with an aperture-defined active area of 0.3 × 0.3 cm^2, were characterized in the air under an Air Mass 1.5 Global (AM 1.5G) solar simulator with an irradiation intensity of 100 mW/cm^2, which was calibrated using a standard crystalline silicon solar cell (Oriel, Newport, USA). For the measurement of I-V characteristics, we obtained the I-V curve through a forward scan (−0.5 to 1.2 V) with a step size of 50 mV.

3. Results and Discussion

Figure 1 illustrates the schematic representation of the magnetron sputtering process used for the deposition of NiO_x and ZnO thin films. Sputtering, a vacuum-based physical vapor deposition (PVD) technique, offers several key advantages

such as high film uniformity, reproducibility, scalability, and precise control over deposition parameters [36] [37]. In this process, an inert gas-typically argon (Ar)-is introduced into a vacuum chamber, where a cathode (also referred to as the "target") is energized to initiate and sustain plasma. The target is composed of the material intended for deposition onto the substrate. When the argon atoms in the plasma lose electrons, they become positively charged ions. These ions are then accelerated toward the negatively charged target, bombarding its surface with sufficient kinetic energy to eject atoms or molecules from the target material. The ejected species form a vapor cloud within the chamber, which travels toward the substrate and condenses to form a uniform thin film. The properties of the films are influenced by several sputtering parameters, such as the type of sputtering gas, sputtering pressure, substrate temperature [38], and the thermal annealing applied to the deposited films [39]. Compared to other deposition techniques such as thermal evaporation, sputtered films generally exhibit superior adhesion to the substrate due to the high-energy impact of the deposited species. Energy Dispersive X-ray (EDX) analysis was employed to quantify the elemental composition, as illustrated in **Figure S1** for NiO_x and **Figure S2** for ZnO thin films. Additionally, reactive sputtering, where oxygen or other reactive gases are introduced, can be employed to deposit compound materials like NiO_x or ZnO directly during the sputtering process.

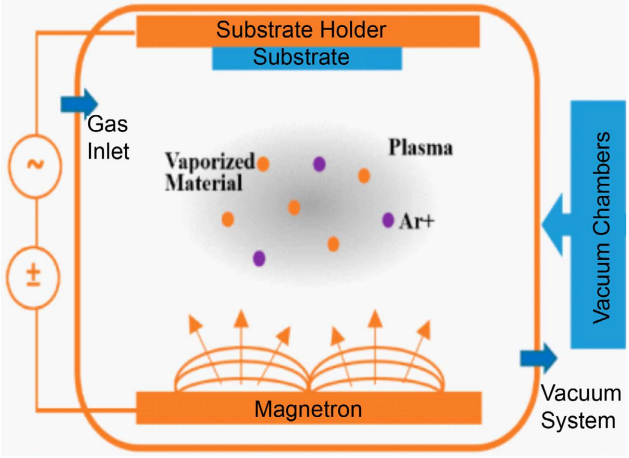

Figure 1. Schematic deposition of NiO_x and ZnO thin films using the magnetron sputtering method.

Figure 2 presents the X-ray diffraction (XRD) patterns of NiO_x, ZnO, $CsPbI_3$ films, and the absorbance spectra of $CsPbI_3$ films. For thin film characterization, Grazing Incidence X-ray Diffraction (GIXRD) was employed instead of symmetric diffraction to restrict X-ray penetration to the film surface and prevent interference from the substrate. It was observed that a longer deposition time was necessary to obtain discernible diffraction peaks. No significant peaks appeared after 30 minutes of deposition on porous Si (p-Si) substrates. However, with one hour of deposition, a prominent diffraction peak around 42˚ was detected for NiO_x,

corresponding to the (200) plane, consistent with previous reports [29] [30] [40]. For ZnO, a single intense peak corresponding to the (100) plane was identified in both recipes studied [39] [41] [42]. The high intensity of this peak, relative to the substrate background, indicates strong crystallinity in the ZnO thin film.

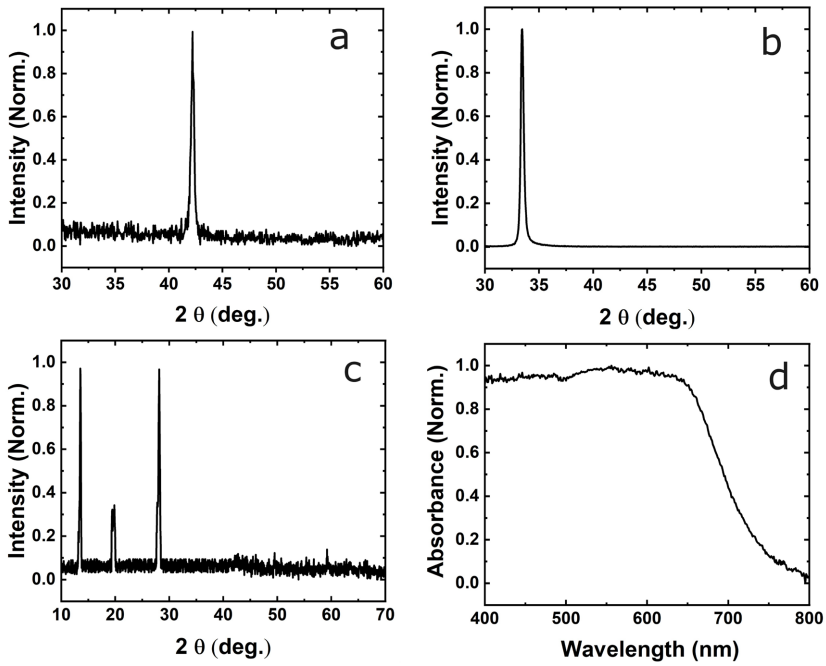

Figure 2. X-ray pattern of (a) NiO_x; (b) ZnO; (c) $CsPbI_3$ films; (d) Absorbance of $CsPbI_3$ films.

The $CsPbI_3$ films demonstrated in **Figure 2(c)** have high sensitivity to ambient humidity during formation. $CsPbI_3$ films were prepared under ambient air conditions at a relative humidity of approximately 28% and a temperature of ~24˚C. At humidity levels above 40%, the films rapidly transitioned to the yellow, non-photoactive δ-phase. This transformation was confirmed by XRD, which showed peaks distinct from those of the black cubic α-phase. When the relative humidity was maintained below 30%, the stable photoactive α-phase was preserved, displaying characteristic diffraction peaks at 13.52˚ and 28˚, corresponding to the (100) and (200) planes, respectively [34] [43]. Further structural analysis was conducted using the Williamson-Hall (W-H) method, which accounts for both size- and strain-induced broadening of XRD peaks. The total peak broadening (β_{total}) can be expressed as:

$$\beta_{total} = \beta_{size} + \beta_{strain}$$

The Scherrer equation was applied to estimate the average crystallite size (D):

$$D = \frac{K\lambda}{\beta_{total}} \cdot \frac{1}{\cos\theta}$$

where D is the average crystallite size, K is the shape factor (~0.9), λ is the X-ray wavelength, β_{total} is the full width at half maximum (FWHM) in radians (corrected

for instrumental broadening), and θ is the Bragg angle.

The strain-induced broadening is described as:

$$\beta_{strain} = 4\varepsilon \cdot \tan\theta$$

From the XRD data, the average crystallite size of $CsPbI_3$ thin films ranged from 23.12 nm to 31.62 nm, indicating well-formed grains. Crystallite sizes of ZnO and NiO_x thin films were found to be 22.84 nm and 24.18 nm, respectively.

Micro strain values were calculated to be 9.2×10^{-3} for $CsPbI_3$, 5.96×10^{-3} for ZnO, and 3.93×10^{-3} for NiO_x. Corresponding dislocation densities were determined as 1.89×10^{-3}, 2.02×10^{-3}, and 1.71×10^{-3} nm^{-2}, respectively. These findings affirm the good crystallinity in sputtered thin films, crucial for high-performance optoelectronic applications.

The introduction of PAN did not alter the band gap of the $CsPbI_3$ samples, according to their ultraviolet-visible absorption spectra, as shown in **Figure 2(d)**. The $CsPbI_3$ film's absorption margins were around 740 nm (1.67 eV), and this value was comparable with the material's theoretically calculated band gap.

Figure 3 shows the surface morphology of the NiO_x, ZnO, and $CsPbI_3$ thin films, as observed using a ZEISS Sigma VP Scanning Electron Microscope (SEM). For the NiO_x film, SEM images reveal a uniform layer of densely packed nanograins covering the ITO substrate. These grains exhibited an average size of approximately 22 nm. With increased deposition time, the NiO_x surface morphology became more homogeneous, indicating improved film coverage and reduced surface defects, factors beneficial for efficient hole transport in solar cell applications. The ZnO film displayed a fine granular texture, consisting of a well-distributed network of nearly spherical particles with an average diameter of around 20 nm. Grain size was found to increase with longer deposition times, which suggests enhanced crystal growth and packing density during film formation.

For the $CsPbI_3$ film, EDX analysis was used to quantify the elemental composition, as illustrated in **Figure S3**, and the compositional data are summarized in **Table S1**. The $CsPbI_3$ perovskite film exhibited larger grain sizes and fewer grain boundaries, implying a reduced density of trap states and improved charge transport. In contrast, the Polyacrylonitrile (PAN)-assisted film had a smoother, more compact surface with minimized pinhole formation. Surface roughness measurements using a Mahr Mcsurf 300 C profilometer confirmed these observations, with the PAN-assisted film showing a roughness of 18 nm. Overall, the SEM analysis confirms that optimized deposition parameters and surface additives can significantly enhance film uniformity, grain size, and morphological integrity-all critical factors for achieving high-performance and stable perovskite PSCs.

Figure 4 illustrates the surface topography of the transport layers, both two-dimensional and three-dimensional, obtained using Atomic Force Microscopy (AFM). The surface morphology and roughness of these films were analyzed to understand their suitability as transport layers in perovskite SCs. For NiO_x films, deposition durations of 10, 30, 60, and 240 min were studied. A clear trend was observed where film thickness increased nearly linearly with deposition time,

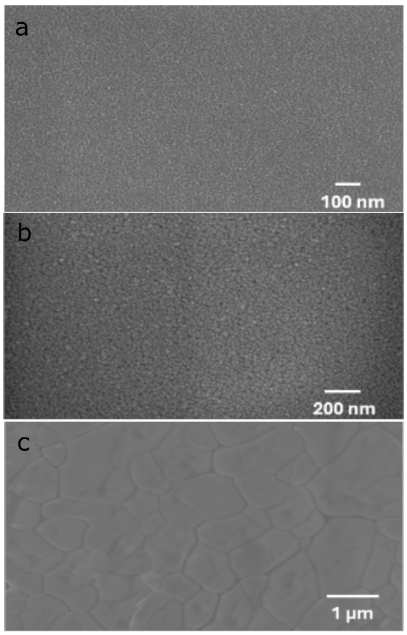

Figure 3. Surface morphologies of (a) NiO_x; (b) ZnO; (c) $CsPbI_3$ films analyzed by scanning electron microscopy.

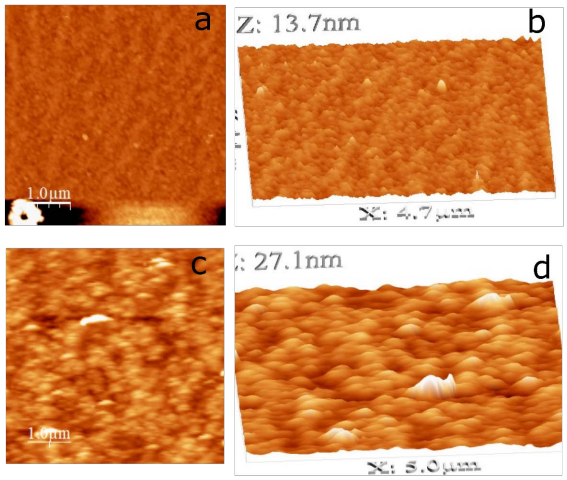

Figure 4. Surface topography of (a) two-dimensional and (b) three-dimensional NiO_x; (c) two-dimensional and (d) three-dimensional ZnO thin films analyzed by atomic force microscopy.

yielding values of 35 nm, 50 nm, 75 nm, and 200 nm, respectively. Correspondingly, the surface roughness decreased with time, from 1.15 nm for the 10-minute film to 0.77 nm for the 240-minute film, as shown in **Figure 4(b)**. The smoother surfaces observed at longer deposition times are beneficial, as they provide a more uniform platform for perovskite layer growth, reducing the chances of pinhole formation and improving device performance. In the AFM images, NiO_x films showed a granular texture with fine, evenly distributed grains. The uniformity and

smoothness improved with longer sputtering durations, indicating better film quality and coverage, and optimized the deposition time to 100 min.

Similarly, for ZnO films, four deposition conditions were tested: high-pressure sputtering at 5, 30, and 60 minutes, and low-pressure sputtering at 60 minutes. The resulting film thicknesses were 25 nm, 80 nm, 180 nm, and 250 nm, respectively. The ZnO surface morphology was characterized by densely packed, spherical grains across all conditions. AFM confirmed that both high- and low-pressure recipes produced well-formed films, but longer sputtering times increased both grain size and film thickness, contributing to denser and smoother films. Surface roughness values for ZnO also showed improvement with increased deposition time, and the minimum roughness of 3.4 nm was observed for the deposition time of 60 minutes, as shown in **Figure 4(d)**. The compact and uniform grain distribution in ZnO films is crucial for ensuring effective electron transport and minimizing recombination losses in the solar cell architecture [44]. Overall, the AFM and profilometry data confirm that sputtering deposition provides controllable and high-quality thin films of NiO_x and ZnO, with tunable roughness and thickness, both essential parameters for optimizing the interface quality in PSCs.

The schematic diagram of the planar p-i-n solar cell configuration (ITO/NiO_x-/$CsPbI_3$/ZnO/Au) illustrates the planar structure of the device as shown in **Figure 5(a)**. Indium tin oxide (ITO) serves as the transparent conducting anode. NiO_x acts as the hole transport layer (p-type), facilitating hole extraction. The central layer, $CsPbI_3$, is a perovskite material responsible for light absorption and charge generation. ZnO functions as the electron transport layer (n-type), enabling electron extraction. Finally, gold (Au) forms the top electrode, completing the circuit for charge collection. This architecture promotes efficient charge separation and collection in perovskite solar cells. The energy band diagram of this planar device is shown in **Figure 5(b)**. The work functions of ITO (used as a front contact) and Au (used as a back contact) were −4.6 eV and −5.1 eV, respectively [45] [46]. The lowest unoccupied molecular orbital (LUMO) levels and the highest occupied molecular orbital (HOMO) levels of the ZnO, $CsPbI_3$, and NiO_x were −4.1 eV, −3.9 eV, and −1.5 eV, and −7.4 eV, −5.6 eV, and −5.2 eV, respectively [47]-[50]. Through this optimized energy band alignment, the electrons and holes generated in the $CsPbI_3$ absorption layer can efficiently move to the Au electrode and ITO electrode, respectively. **Figure 5(c)** shows the current density-voltage (J-V) characteristics of the device. The devices show a very low leakage current density of 5 $nA{\cdot}cm^{-2}$, as shown in **Figure S4**, and the enhancement of approximately four orders under 1 Sun illumination. The performance parameters, including open circuit voltage (V_{oc}), short-circuit density (J_{sc}), fill factor (FF), and PCE, were 0.82 V, 14.25 mA/cm^2, 67%, and 7.8%, respectively. For comparison, recent studies employing a similar device architecture have reported power conversion efficiencies of up to 12.2% for $CsPbI_3$-based perovskite solar cells, indicating that while higher efficiencies are achievable, they often rely on more tightly controlled processing or additional interface optimization [51]. From the J-V curve analysis, the series

and shunt resistances were determined to be 8.12 Ω·cm^2 and 1778 Ω·cm^2, respectively. The J_{sc} and V_{oc} both show consistency with the dark and illumination characteristics.

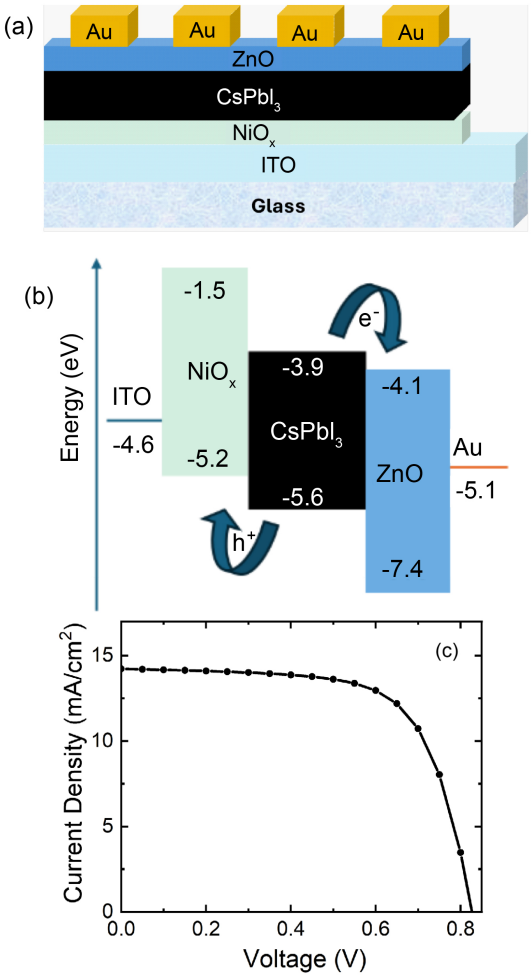

Figure 5. (a) Schematic diagram of the planar p-i-n solar cell configuration (ITO/NiO_x/$CsPbI_3$/ZnO/Au); (b) Energy level diagram of the device, (c) J~V characteristics of the solar cell.

4. Conclusion

In summary, both electron and hole transport layers were deposited via magnetron sputtering, and the transport and photoactive layers were optimized through XRD, UV-Visible spectroscopy, SEM, and AFM analyses, with the final device characterized using a solar simulator to evaluate its overall performance. The photoactive $CsPbI_3$ layer, deposited via a spin coating solution process, exhibited strong absorbance in the 400 - 750 nm range with a band gap of 1.67 eV, and XRD analysis confirmed the crystalline structure of both the transport and active layers. Surface morphology and AFM analyses revealed that $CsPbI_3$ formed large, well-covered grains with low surface roughness. Both transport layers displayed low surface roughness values of 0.7 nm and 3.4 nm, suggesting excellent interfacial con-

tact with other layers. This approach resulted in devices achieving a power conversion efficiency of 7.8%, an open-circuit voltage of 0.82 V, a fill factor of 0.67, and a short-circuit current density of 14.25 $mA \cdot cm^{-2}$, with optimized layer thicknesses of 40 nm (NiO_x), 420 nm ($CsPbI_3$), 40 nm (ZnO), and 80 nm (Au). Our deposition technique not only demonstrates reliable performance but also provides a pathway to explore alternative device architectures. Our study establishes a sputter-compatible, ambient-air-processed $CsPbI_3$ device architecture in which a PAN interfacial layer enhances oxide-perovskite integration, advancing prior reports by prioritizing fabrication tolerance, interface stability, and a reliable "vacuum-solution-vacuum" process, thereby demonstrating sputtering as a scalable and robust fabrication route rather than a record-efficiency approach. Moreover, the methodology described here is anticipated to advance the scalability and reproducibility of solar cell fabrication, paving the way for broader application and industrial relevance. Future enhancements will investigate the influence of substrate temperature during deposition and post-deposition annealing treatments on film crystallinity and interface quality. These studies are expected to further improve device efficiency and stability by optimizing microstructural and electronic properties.

Author Contributions

S.D.: Conceptualization, Methodology, Formal Analysis, Investigation, and Writing-Review & Editing; **M.A.K.S.:** Conceptualization, Formal Analysis, Investigation, Writing-Original Draft, and Writing-Review & Editing; **M.S.I.:** Formal Analysis and Writing-Review & Editing; **M.J.U:** Supervision, Resources, and Writing-Review & Editing; **H.H.:** Supervision, Resources, Writing-Review & Editing, Project Administration, and Funding Acquisition. All authors have read and agreed to the published version of the manuscript.

Funding

This research is supported in part by the National Science Foundation (NSF) under Grant No. 1229523, and by the US Army Research Office W911NF-14-1-0100.

Conflicts of Interest

The authors declare no conflicts of interest regarding the publication of this paper.

References

[1] Green, M.A., Dunlop, E.D., Yoshita, M., *et al.* (2025) Solar Cell Efficiency Tables (Version 66). *Progress in Photovoltaics*: *Research and Applications*, **33**, 795-810.

[2] NREL (2025) Best Research-Cell Efficiency Chart. https://www.nlr.gov/pv/cell-efficiency

[3] Shockley, W. and Queisser, H.J. (1961) Detailed Balance Limit of Efficiency of *p-n* Junction Solar Cells. *Journal of Applied Physics*, **32**, 510-519. https://doi.org/10.1063/1.1736034

[4] Kojima, A., Teshima, K., Shirai, Y. and Miyasaka, T. (2009) Organometal Halide Perovskites as Visible-Light Sensitizers for Photovoltaic Cells. *Journal of the American*

Chemical Society, **131**, 6050-6051. https://doi.org/10.1021/ja809598r

[5] Sheikh, M.A.K., Abdur, R., Singh, S., Kim, J., Min, K., Kim, J., *et al*. (2018) Effects of Chlorine Contents on Perovskite Solar Cell Structure Formed on CdS Electron Transport Layer Probed by Rutherford Backscattering. *Electronic Materials Letters*, **14**, 700-711. https://doi.org/10.1007/s13391-018-0084-4

[6] Yi, A., Chae, S., Luong, H.M., Lee, S.H., Lee, H., Yoon, H., *et al*. (2024) Room-Temperature-Processed Perovskite Solar Cells Surpassing 24% Efficiency. *Joule*, **8**, 2087-2104. https://doi.org/10.1016/j.joule.2024.04.002

[7] Panidi, J., Georgiadou, D.G., Schoetz, T. and Prodromakis, T. (2022) Advances in Organic and Perovskite Photovoltaics Enabling a Greener Internet of Things. *Advanced Functional Materials*, **32**, Article 2200694. https://doi.org/10.1002/adfm.202200694

[8] Afroz, M., Ratnesh, R.K., Srivastava, S. and Singh, J. (2025) Perovskite Solar Cells: Progress, Challenges, and Future Avenues to Clean Energy. *Solar Energy*, **287**, Article 113205. https://doi.org/10.1016/j.solener.2024.113205

[9] Swain, B.S., Sheikh, M.A.K., Singh, S., Abdur, R., Jeong, D. and Lee, J. (2018) $CH_3NH_3PbBr_3$ Nanocubes-Array for Solar Cell Application. *Materials Science in Semiconductor Processing*, **74**, 361-368. https://doi.org/10.1016/j.mssp.2017.10.050.

[10] Singh, S., Abdur, R., Sheikh, M.A.K., Swain, B.S., Song, J., Kim, J., *et al*. (2024) Selective Spin Dewetting for Perovskite Solar Modules Fabricated on Engineered Au/ITO Substrates. *Nanomaterials*, **14**, Article 424. https://doi.org/10.3390/nano14050424

[11] Straus, D.B., Guo, S., Abeykoon, A.M. and Cava, R.J. (2020) Understanding the Instability of the Halide Perovskite $CsPbI_3$ through Temperature-Dependent Structural Analysis. *Advanced Materials*, **32**, e2001069. https://doi.org/10.1002/adma.202001069

[12] Niu, G., Guo, X. and Wang, L. (2015) Review of Recent Progress in Chemical Stability of Perovskite Solar Cells. *Journal of Materials Chemistry A*, **3**, 8970-8980. https://doi.org/10.1039/c4ta04994b

[13] Wang, J., Che, Y., Duan, Y., Liu, Z., Yang, S., Xu, D., *et al*. (2023) 21.15%-Efficiency and Stable γ-$CsPbI_3$ Perovskite Solar Cells Enabled by an Acyloin Ligand. *Advanced Materials*, **35**, e2210223. https://doi.org/10.1002/adma.202210223

[14] Chang, X., Fang, J., Fan, Y., Luo, T., Su, H., Zhang, Y., *et al*. (2020) Printable $CsPbI_3$ Perovskite Solar Cells with PCE of 19% via an Additive Strategy. *Advanced Materials*, **32**, e2001243. https://doi.org/10.1002/adma.202001243

[15] Roy, R., Byranvand, M.M., Zohdi, M.R., Magorian Friedlmeier, T., Das, C., Hempel, W., *et al*. (2025) All-Inorganic $CsPbI_2Br$ Perovskite Solar Cells with Thermal Stability at 250˚C and Moisture-Resilience via Polymeric Protection Layers. *Energy & Environmental Science*, **18**, 1920-1928. https://doi.org/10.1039/d4ee02385d

[16] Ferdous, R. and Hashmi, G. (2025) A Comprehensive Device Modeling of Organic-Inorganic Hybrid $CH_3NH_3GeI_3$ Based Perovskite Solar Cell. *Results in Materials*, **25**, Article 100665. https://doi.org/10.1016/j.rinma.2025.100665

[17] Wang, Q., Zheng, X., Deng, Y., Zhao, J., Chen, Z. and Huang, J. (2017) Stabilizing the α-Phase of $CsPbI_3$ Perovskite by Sulfobetaine Zwitterions in One-Step Spin-Coating Films. *Joule*, **1**, 371-382. https://doi.org/10.1016/j.joule.2017.07.017

[18] Wang, Y., Chen, Y., Zhang, T., Wang, X. and Zhao, Y. (2020) Chemically Stable Black Phase $CsPbI_3$ Inorganic Perovskites for High-Efficiency Photovoltaics. *Advanced Materials*, **32**, Article 2001025. https://doi.org/10.1002/adma.202001025

[19] Jiang, Y., Qiu, L., Juarez-Perez, E.J., Ono, L.K., Hu, Z., Liu, Z., *et al*. (2019) Reduction of Lead Leakage from Damaged Lead Halide Perovskite Solar Modules Using Self-

Healing Polymer-Based Encapsulation. *Nature Energy*, **4**, 585-593. https://doi.org/10.1038/s41560-019-0406-2

[20] Jiang, Q., Zhao, Y., Zhang, X., Yang, X., Chen, Y., Chu, Z., *et al.* (2019) Surface Passivation of Perovskite Film for Efficient Solar Cells. *Nature Photonics*, **13**, 460-466. https://doi.org/10.1038/s41566-019-0398-2

[21] Mehrabian, M., Norouzzadeh, P. and Akhavan, O. (2026) Improving Hybrid Perovskite Solar Cells by Utilization and Optimization of $Cs_2AgBiBr_6$/$MaPbI_3$/$CsSnI_3$ Triple Cascade Structure. *Journal of Power Sources*, **661**, Article 238633. https://doi.org/10.1016/j.jpowsour.2025.238633

[22] Kaur, N., Madan, J., Ramos Jiménez, R.B., Ñacato Estrella, D.R. and Pandey, R. (2025) Tailored Bandgap Grading in $CsSnI_3$-XBr_x All Inorganic Perovskite Solar Cells with 2D MXene Electrodes: A Path to High-Efficiency Photovoltaics. *Solid State Communications*, **397**, Article 115840. https://doi.org/10.1016/j.ssc.2025.115840

[23] Mehrabian, M., Taleb-Abbasi, M. and Akhavan, O. (2025) Comparing the Performances of Cs_2TiBr_6, $Cs_2AgBiBr6$, and Cs_2PtI_6 Halide Compositions in Double Perovskite Photovoltaic Devices. *Materials for Renewable and Sustainable Energy*, **14**, Article No. 38. https://doi.org/10.1007/s40243-025-00311-z

[24] Goje, A.A., Ludin, N.A., Sepeai, S., Su'ait, M.S., Syafiq, U. and Chelvanathan, P. (2026) Enhancing Lead-Free $Cs_3Bi_2I_9$ Flexible Perovskite Solar Cells via Fira. *Solar Energy*, **303**, Article 114130. https://doi.org/10.1016/j.solener.2025.114130

[25] Li, L., Wang, Y., Wang, X., Lin, R., Luo, X., Liu, Z., *et al.* (2022) Flexible All-Perovskite Tandem Solar Cells Approaching 25% Efficiency with Molecule-Bridged Hole-Selective Contact. *Nature Energy*, **7**, 708-717. https://doi.org/10.1038/s41560-022-01045-2

[26] Xie, L., Du, S., Li, J., Liu, C., Pu, Z., Tong, X., *et al.* (2023) Molecular Dipole Engineering-Assisted Strain Release for Mechanically Robust Flexible Perovskite Solar Cells. *Energy & Environmental Science*, **16**, 5423-5433. https://doi.org/10.1039/d3ee02569a

[27] Hwang, K., Jung, Y., Heo, Y., Scholes, F.H., Watkins, S.E., Subbiah, J., *et al.* (2015) Toward Large Scale Roll-to-Roll Production of Fully Printed Perovskite Solar Cells. *Advanced Materials*, **27**, 1241-1247. https://doi.org/10.1002/adma.201404598

[28] Jariwala, S., Singh, T. and Miyasaka, T. (2021) Exploring Sputtering Methods for Scalable Perovskite Photovoltaics. *Solar RRL*, **5**, Article 2000587.

[29] Kim, S., Seok, H., Kim, D., Choi, D., Nam, S., Kim, S., *et al.* (2020) Comparison of NiO_x Thin Film Deposited by Spin-Coating or Thermal Evaporation for Application as a Hole Transport Layer of Perovskite Solar Cells. *RSC Advances*, **10**, 43847-43852. https://doi.org/10.1039/d0ra08776a

[30] Yan, X., Zheng, J., Zheng, L., Lin, G., Lin, H., Chen, G., *et al.* (2018) Optimization of Sputtering NiO Films for Perovskite Solar Cell Applications. *Materials Research Bulletin*, **103**, 150-157. https://doi.org/10.1016/j.materresbull.2018.03.027

[31] Salunkhe, P., A.V, M.A. and Kekuda, D. (2021) Structural, Spectroscopic and Electrical Properties of DC Magnetron Sputtered NiO Thin Films and an Insight into Different Defect States. *Applied Physics A*, **127**, Article No. 390. https://doi.org/10.1007/s00339-021-04501-0

[32] Wang, X., Ran, X., Liu, X., Gu, H., Zuo, S., Hui, W., *et al.* (2020) Tailoring Component Interaction for Air-Processed Efficient and Stable All-Inorganic Perovskite Photovoltaic. *Angewandte Chemie International Edition*, **59**, 13354-13361. https://doi.org/10.1002/anie.202004256

[33] Yoon, S.M., Min, H., Kim, J.B., Kim, G., Lee, K.S. and Seok, S.I. (2021) Surface Engi-

neering of Ambient-Air-Processed Cesium Lead Triiodide Layers for Efficient Solar Cells. *Joule*, **5**, 183-196. https://doi.org/10.1016/j.joule.2020.11.020

[34] Yu, G., Jiang, K., Gu, W., Zhang, Y., Xu, Y., Xue, T., *et al.* (2022) Stabilizing All-Inorganic $CsPbI_3$ Perovskite Films with Polyacrylonitrile for Photovoltaic Solar Cells. *Energy Advances*, **1**, 62-66. https://doi.org/10.1039/d1ya00068c

[35] Wang, P., Wang, J., Zhang, X., Wang, H., Cui, X., Yuan, S., *et al.* (2018) Boosting the Performance of Perovskite Solar Cells through a Novel Active Passivation Method. *Journal of Materials Chemistry A*, **6**, 15853-15858. https://doi.org/10.1039/c8ta05593a

[36] Greene, J.E. (2017) Review Article: Tracing the Recorded History of Thin-Film Sputter Deposition: From the 1800s to 2017. *Journal of Vacuum Science & Technology A*: *Vacuum*, *Surfaces*, *and Films*, **35**, 05C204. https://doi.org/10.1116/1.4998940

[37] Baptista, A., Silva, F., Porteiro, J., Míguez, J. and Pinto, G. (2018) Sputtering Physical Vapour Deposition (PVD) Coatings: A Critical Review on Process Improvement and Market Trend Demands. *Coatings*, **8**, Article 402. https://doi.org/10.3390/coatings8110402

[38] Pham, T.K.H., Tran, B.Q., Nguyen, K.B., Pham, N.Y.N., Nguyen, T.H.Y., Nguyen, A.H., *et al.* (2025) Oxygen Partial Pressure Effects on Nickel Oxide Thin Films and NiO/Si Diode Performance. *Materials Advances*, **6**, 1719-1725. https://doi.org/10.1039/d4ma01113a

[39] Simeonov, S., Szekeres, A., Spassov, D., Anastasescu, M., Stanculescu, I., Nicolescu, M., *et al.* (2021) Investigation of the Effects of Rapid Thermal Annealing on the Electron Transport Mechanism in Nitrogen-Doped ZnO Thin Films Grown by RF Magnetron Sputtering. *Nanomaterials*, **12**, Article 19. https://doi.org/10.3390/nano12010019

[40] Lu, Y.M., Hwang, W.S. and Yang, J.S. (2002) Effects of Substrate Temperature on the Resistivity of Non-Stoichiometric Sputtered NiO_x Films. *Surface and Coatings Technology*, **155**, 231-235. https://doi.org/10.1016/s0257-8972(02)00037-3

[41] Tvarozek, V., Novotny, I., Sutta, P., Flickyngerova, S., Schtereva, K. and Vavrinsky, E. (2007) Influence of Sputtering Parameters on Crystalline Structure of ZnO Thin Films. *Thin Solid Films*, **515**, 8756-8760. https://doi.org/10.1016/j.tsf.2007.03.125

[42] Fawey, M.H., El-Moula, A.A.A., El-Hossary, F.M., Hashem, T. and El-Kassem, M.A. (2025) Optical and Structural Properties of ZnO/TiO_2 Bilayer Thin Films Deposited by Pulsed DC Magnetron Sputtering. *Journal of Materials Science*: *Materials in Electronics*, **36**, Article No. 764. https://doi.org/10.1007/s10854-025-14703-4

[43] Zolfaghari, Z., Hassanabadi, E., Pitarch-Tena, D., Yoon, S.J., Shariatinia, Z., van de Lagemaat, J., *et al.* (2018) Operation Mechanism of Perovskite Quantum Dot Solar Cells Probed by Impedance Spectroscopy. *ACS Energy Letters*, **4**, 251-258. https://doi.org/10.1021/acsenergylett.8b02157

[44] Mehrabian, M., Taleb-Abbasi, M. and Akhavan, O. (2023) Effects of Electron Transport Layer Type on the Performance of Pb-Free $Cs_2AgBiBr_6$ Double Perovskites: A SCAPS-1D Solar Simulator-Based Study. *Environmental Science and Pollution Research*, **30**, 118754-118763. https://doi.org/10.1007/s11356-023-30732-0

[45] Song, Y., Yan, L., Zhou, Y., Song, B. and Li, Y. (2015) Inverted Solar Cells: Lowering the Work Function of ITO by Covalent Surface Grafting of Aziridine: Application in Inverted Polymer Solar Cells. *Advanced Materials Interfaces*, **2**, Article 1400397. https://doi.org/10.1002/admi.201500051

[46] Sawicka-Chudy, P., Starowicz, Z., Wisz, G., Yavorskyi, R., Zapukhlyak, Z., Bester, M.,

et al. (2019) Simulation of TiO_2/CuO Solar Cells with SCAPS-1D Software. *Materials Research Express*, **6**, Article 085918. https://doi.org/10.1088/2053-1591/ab22aa

[47] Bhavsar, K. and Lapsiwala, P.B. (2021) Numerical Simulation of Perovskite Solar Cell with Different Material as Electron Transport Layer Using SCAPS-1D Software. *Semiconductor Physics, Quantum Electronics and Optoelectronics*, **24**, 341-347. https://doi.org/10.15407/spqeo24.03.341

[48] Martínez, N., Pinzón, C., Casas, G., *et al*. (2020) Computational Study of Inverted All-Inorganic Perovskite Solar Cells Based on $CsPbI_xBr_{3-x}$ Absorber Layer with Band Gap of 1.78 eV. *Energy*, **2020**, 1-13.

[49] Hossain, M.I., Alharbi, F.H. and Tabet, N. (2015) Copper Oxide as Inorganic Hole Transport Material for Lead Halide Perovskite Based Solar Cells. *Solar Energy*, **120**, 370-380. https://doi.org/10.1016/j.solener.2015.07.040

[50] Anwar, F., Mahbub, R., Satter, S.S. and Ullah, S.M. (2017) Effect of Different HTM Layers and Electrical Parameters on ZnO Nanorod-Based Lead-Free Perovskite Solar Cell for High-Efficiency Performance. *International Journal of Photoenergy*, **2017**, 1-9. https://doi.org/10.1155/2017/9846310

[51] Deng, W., Li, J., Jin, J., Mishra, D.D., Xin, J., Lin, L., *et al*. (2020) Fast and Low Temperature Processed $CsPbI_3$ Perovskite Solar Cells with ZnO as Electron Transport Layer. *Journal of Power Sources*, **480**, Article 229134. https://doi.org/10.1016/j.jpowsour.2020.229134

Abbreviations

Solar Cells (SCs), Perovskite Solar Cells (PSCs), Power Conversion Efficiency (PCE), Hole Transport Layer (HTL), Electron Transport Layer (ETL), Physical Vapor Deposition (PVD), Energy Dispersive X-Ray (EDX), X-Ray Diffraction (XRD), Grazing Incidence X-Ray Diffraction (GIXRD), Scanning Electron Microscope (SEM), Polyacrylonitrile (PAN), Atomic Force Microscopy (AFM).

Appendix

Energy Dispersive X-Ray (EDX) Spectroscopy

The NiOx film was slightly more dominated by Nickel. It was expected due to the well-known fact that achieving a stoichiometric ratio of NiOx is difficult. If the film appears green, the p-type character of the film is preserved and good enough for photovoltaic application. It should also be taken into consideration that oxygen, as a sputtering gas, was not provided in our deposition.

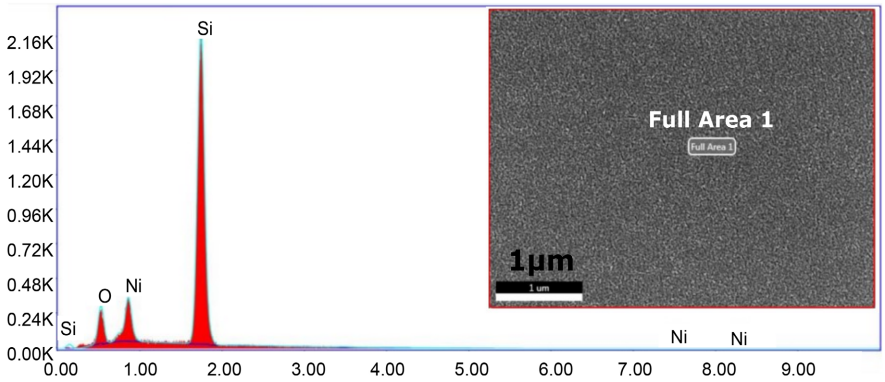

Figure S1. EDX analysis of NiO_x thin film.

Although the atomic percentage for the ZnO was almost equally distributed between the two elements, as summarized in Table S1, it was also slightly dominated by the Zn for the same reason, *i.e.*, not using oxygen as a sputtering gas.

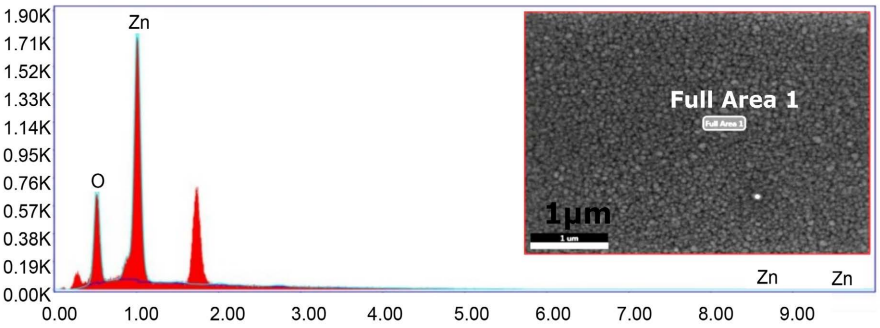

Figure S2. EDX analysis of ZnO thin film.

Table S1. eZAF smart quant results.

Compounds	Element	Weight (%)	Atomic (%)
NiO_x	O	7.18	12.53
	Ni	9.43	4.49
	Si	83.39	82.98
ZnO	O	18.66	48.38
	Zn	81.34	51.62

Continued

$CsPbI_3$	**C**	**7.97**	**40.77**
	N	4.82	21.17
	I	21.00	10.17
	O	1.92	7.38
	Cs	8.70	4.02
	Pb	55.59	16.49

Although the signals were noisy, the EDX report of the $CsPbI_3$ perovskite shows the presence of all the elemental components of $CsPbI_3$ perovskite and polyacrylonitrile (PAN), *i.e.*, Cs, Pb, I, C, N, and O. The appearance of Carbon, Oxygen, and Nitrogen also confirmed that PAN is not serving here as an additive. Instead, it is taking the role of a defect passivator by staying on the film surface.

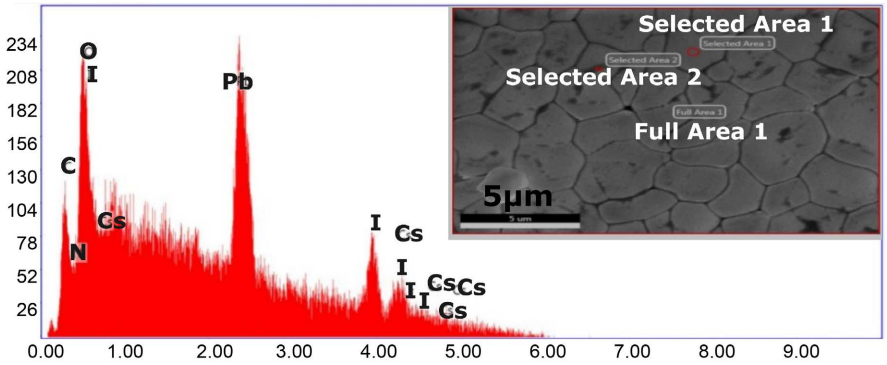

Figure S3. EDX analysis of $CsPbI_3$ thin film.

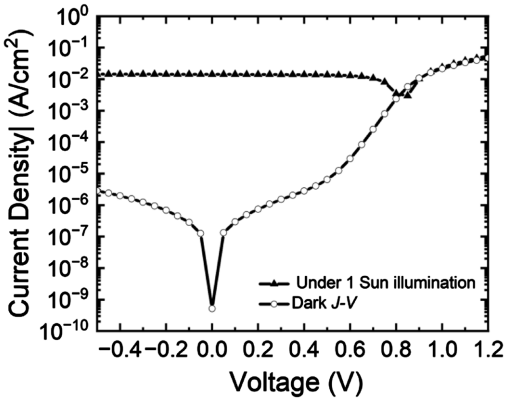

Figure S4. Dark and illuminated I-V characteristics.